

Optical Control of Plasmonic Hot Carriers in Graphene

Jadidi, M. M.; Daniels, K. M.; Myers-Ward, R. L.; Gaskill, D. K.; König-Otto, L. C.;
Winnerl, S.; Sushkov, A. B.; Drew, H. D.; Murphy, T. E.; Mittendorff, M.;

Originally published:

January 2019

ACS Photonics 6(2019), 302-307

DOI: <https://doi.org/10.1021/acsp Photonics.8b01499>

Perma-Link to Publication Repository of HZDR:

<https://www.hzdr.de/publications/Publ-27951>

Release of the secondary publication
on the basis of the German Copyright Law § 38 Section 4.

Terahertz-Induced Hot Carrier Plasmon Frequency Shift in Graphene Ribbons

M. MEHDI JADIDI^{1,2,*}, KEVIN M. DANIELS^{1,3}, RACHAEL L. MYERS-WARD³, D. KURT GASKILL³, JACOB C. KÖNIG-OTTO^{4,5}, STEPHAN WINNERL⁴, ANDREI B. SUSHKOV⁶, H. DENNIS DREW⁶, THOMAS E. MURPHY¹, AND MARTIN MITTENDORFF^{1,7}

¹Institute for Research in Electronics & Applied Physics, University of Maryland, College Park, Maryland, 20740, USA

²Department of Applied Physics and Applied Mathematics, Columbia University, New York, NY 10027, USA

³U. S. Naval Research Laboratory, Washington, DC 20375, USA

⁴Helmholtz-Zentrum Dresden-Rossendorf, P.O. Box 510119, 01314 Dresden, Germany

⁵Technische Universität Dresden, 01062 Dresden, Germany

⁶Center for Nanophysics and Advanced Materials, University of Maryland, College Park, Maryland 20742, USA

⁷Fakultät für Physik, Universität Duisburg-Essen, 47057 Duisburg, Germany

*Corresponding author: mj2838@columbia.edu

Compiled September 17, 2018

We present terahertz pump-probe measurements of sub-wavelength graphene ribbons that show a strong, optically-induced nonlinearity (of order 10%) in an atomically thin layer at a plasmon frequency of 3.9 THz. Measurements taken above and below the plasmon resonance frequency clearly demonstrate that the nonlinearity results from an optically-induced red-shift in the plasmon resonance, which is a signature of hot carriers in the graphene. Unlike conventional thermal nonlinearities, which are typically slow and ill-suited for optical switching and processing, the observed nonlinearity exhibits few picoseconds response time, which is limited only by the cooling rate of hot electrons. The measurements confirm theoretical predictions about the nature of the THz nonlinearity in graphene, and illustrate how sub-wavelength patterns can be engineered to produce atomically thin nonlinear materials in the terahertz regime.

© 2018 Optical Society of America under the terms of the [OSA Open Access Publishing Agreement](#)

OCIS codes: (190.4400) Nonlinear optics, materials; (160.4236) Nanomaterials; (250.5403) Plasmonics; (240.4350) Nonlinear optics at surfaces; (300.6495) Spectroscopy, terahertz;

<http://dx.doi.org/10.1364/optica.XX.XXXXXX>

1. INTRODUCTION

Graphene has been widely studied as an atomically thin nonlinear material that can be added or incorporated into other active or passive optical devices. In the visible and near-infrared regime, the linear and nonlinear optical properties of graphene are governed by the interband response, which is extremely broadband because of graphene's gapless, Dirac dispersion relation. Several nonlinear effects have been observed in graphene, including saturable absorption from Pauli blocking[1–3], third-harmonic generation[4, 5], and four-wave mixing[6, 7], although

in many cases the cumulative nonlinear efficiency is severely limited by the monolayer film thickness. Indeed, the first and most prevalent application of graphene as a nonlinear material remains as a saturable absorber in mode-locked lasers — an application that requires only a small fractional change in absorption[8, 9]. In the terahertz spectral regime, by contrast, the conductivity of graphene is governed by intraband absorption, which is well-described by the Drude model. Graphene's unusual thermal properties, including small electron heat capacity and weak electron-phonon coupling, mean that the electrons responsible for the Drude absorption can be efficiently heated,

thereby producing a hot-carrier nonlinearity that is absent or weak in conventional materials[10–13]. As the hot carriers in graphene cool down on a picosecond timescale, this nonlinearity can even be exploited for efficient harmonic generation in the THz regime [14].

The light-matter interaction in many materials can be tuned and controlled by introducing plasmonic structures [15], which also results in an increased nonlinear response [16]. When graphene is patterned into micron-scale ribbons, the electrons can collectively oscillate at a resonant frequency that depends on both the dimensions and the carrier concentration. These plasmon resonances can be tuned electrically or lithographically throughout the terahertz regime. When these graphene ribbons are illuminated at the resonant frequency, there is a significant increase in the absorption, which is accompanied by a dramatic electric field enhancement in the immediate vicinity of the ribbons [17–21]. Both effects can lead to an increase in the hot-carrier nonlinear interaction[22]. A very recent theoretical study by Cox and Abajo [23] confirms that hot-carrier effects dominate the nonlinearity in graphene plasmons.

In this study, we pattern graphene ribbons from quasi-freestanding epitaxial bilayer graphene that is produced by thermal decomposition of silicon carbide and hydrogen intercalation[24, 25]. This process yields wafer-scale graphene with simultaneously high carrier mobility and concentration – conditions that are ideal for producing a sharp, strong plasmonic resonance[26]. The samples were measured using narrow-band THz pulses from a free-electron laser, which were tuned across the plasmon resonance in order to probe the nature of the enhanced nonlinear response. Our measurements reveal a strong ($\sim 10\%$) and fast (~ 9 ps) THz-induced change in transmission that is associated with an optically-induced red-shift of the plasmon resonance caused by hot carriers.

2. FABRICATION

The epitaxial graphene used in these experiments was synthesized by sublimation of silicon from a $\approx \text{cm}^{-2}$ coupon cut from a 6H-silicon carbide (SiC) wafer (II-VI, Inc.) and subsequent graphitization of carbon, resulting in the structure depicted in Fig 1(a). Unlike conventional exfoliated or CVD-grown graphene, this process produces large-area wafer-scale graphene films with high electrical and morphological uniformity needed for these experiments[27]. The reconstructed carbon buffer layer, which is bound to the SiC, increases the electron-phonon coupling and thereby limits the mobility due to the increased scattering rate of as-grown graphene[25, 28–30]. Using a process of high-temperature hydrogen intercalation, the Si dangling bonds of the SiC are passivated with hydrogen, as shown in Fig 1(b), which decouples the buffer layer from the SiC by converting it into a second layer under the first layer of graphene; the resulting combination is Bernal stacked. This quasi-freestanding bilayer epitaxial graphene has a four-fold increase in carrier mobility, and a corresponding narrowing of the plasmon linewidth[26].

The red curve in Fig. 2 shows the transmission spectrum of the unpatterned bilayer graphene, which was measured using Fourier transform infrared spectroscopy (FTIR) and normalized relative to that of a bare SiC substrate. The superposed dashed line in Fig. 2 shows the calculated transmission spectrum obtained from the Drude model, from which we estimate the carrier density and mobility to be $n = 9.0 \times 10^{12} \text{ cm}^{-2}$ and $\mu_c = 3600 \text{ cm}^2 \text{ V}^{-1} \text{ s}^{-1}$, respectively. These values are in substantial agreement with electrical Hall measurements.

The graphene was patterned via electron-beam lithography and subsequent oxygen plasma etching to produce ribbons with width $w = 900 \text{ nm}$ and a periodicity of $\Lambda = 1200 \text{ nm}$. The blue curve in Fig. 2 is the measured THz transmission spectrum of the ribbons, which shows strong (35%) extinction at the plasmon resonant frequency of 3.9 THz when the illumination is polarized perpendicular to the ribbons. The transmission spectrum of the graphene ribbons can be modeled using the Drude-Lorentz model[22], which predicts a Lorentzian dip in transmission centered at the plasmon frequency, indicated by the blue dashed line. The transmission spectrum of the graphene ribbons was calculated using the previously determined mobility and carrier concentration, the plasmon frequency served as a free parameter in the Drude-Lorentz formula.

3. NONLINEAR MEASUREMENT

The nonlinear response of the graphene sample was measured using a free-electron laser (FELBE facility, located at Helmholtz-Zentrum Dresden-Rossendorf), which produces high-power pulses with a repetition rate of 13 MHz that can be freely tuned throughout the THz range. Importantly, the spectral width of the FEL source in our experiments was approximately 30 GHz, which is much smaller than the plasmon linewidth shown in Fig. 2. We note that table-top pulsed THz sources based on optical rectification of femtosecond pulses or photoconductive emission produce multi-octave broadband THz pulses that can not efficiently excite the narrow-band plasmon resonance of this sample. Nearly co-linear pump and probe beams were focused to an approximate spot size of 0.7 mm onto the sample using an off-axis parabolic mirror, and transmitted probe beam power was recorded using a Si bolometer as a function of the time delay between pump and probe pulse. In order to observe the dynamical resonance shift, pump-probe measurements were conducted at five different frequencies chosen to be below and above the plasmon resonance, indicated by the vertical lines in Fig. 2: 2.0, 2.6, 3.9, 4.4, and 4.9 THz. The sample was held in a helium cryostat at a lattice temperature of 15 K throughout the measurements.

The strongest pump-induced transient is observed when the photon frequency is resonant with the plasmon frequency at 3.9 THz, and both pump and probe are co-polarized perpendicular to the graphene ribbons. In this case, we observe a pump-induced increase in the transmission, as shown in Fig. 3a. The highest measured change was 9%, which was observed at a fluence of $1.8 \mu\text{J cm}^{-2}$. The observed change in transmission increases with the pump fluence approximately in proportion to $F^{1/2}$, as shown in Fig. 3b. We note that typical nonlinear effects scale quadratically or cubically with intensity. As for the plasmonic nonlinearity the change in transmission scales with the square root of the intensity, it is already strong at comparably low fluence. Transmission changes of more than 5% are achieved at fluences of only $0.5 \mu\text{J cm}^{-2}$.

For the nonlinear measurements presented in Fig. 3, both the pump and the probe are simultaneously resonant with the structure, which yields a compounded nonlinear enhancement: not only is the pump absorption resonantly increased, thereby leading to the strongest possible carrier heating, but the probe pulse is also tuned to the resonance, and is therefore very sensitive to induced changes in the plasmon frequency or linewidth. To better resolve the nature of the plasmonic nonlinearity, additional measurements were conducted at frequencies below and above the plasmon resonance, indicated by the vertical lines in Fig. 2.

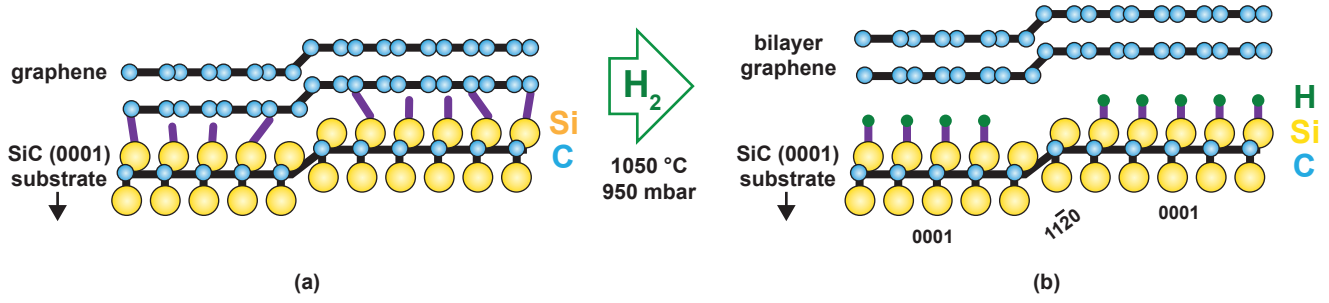


Fig. 1. (a) Diagram of monolayer epitaxial graphene synthesized by the sublimation of silicon from the (0001) surface of SiC, prior to hydrogen intercalation. (b) After hydrogen intercalation, the Si dangling bonds of SiC are passivated with hydrogen and the buffer layer is promoted, forming quasi-freestanding bilayer graphene (QFS BLG) with significantly higher mobility and plasmon lifetime. Hydrogen intercalation only affects the terraces (0001) due to a lack of Si dangling bonds on the (1120) steps of SiC.

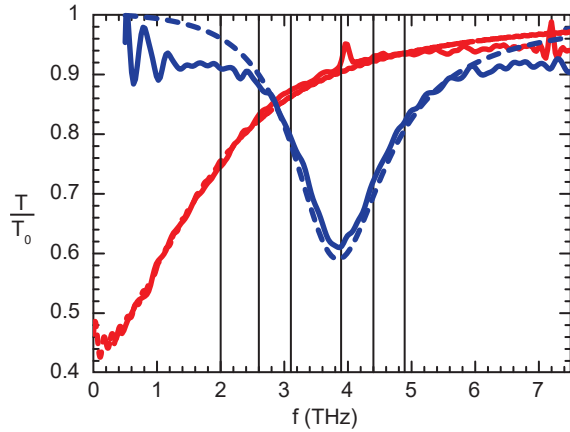


Fig. 2. Measured (solid) and simulated (dashed) transmission spectrum of unpatterned graphene (red) and patterned graphene ribbons (blue). The vertical lines indicate the five THz frequencies above and below resonance at which nonlinear response of the sample was measured: 2.0, 2.6, 3.9, 4.4, and 4.9 THz.

For these measurements, the pump polarization was adjusted to be parallel to the graphene ribbons – a condition that excludes the resonant excitation of plasmons. Under these conditions, the pump pulse heats the free carriers in the graphene through conventional Drude absorption, which only weakly depends on frequency over the spectral range considered. The probe polarization, meanwhile, was maintained perpendicular to the ribbons, thereby probing the plasmon resonance.

Fig. 4a shows the observed pump-probe response at the five frequencies considered. Because the pump is no longer resonant with the structure, the peak observed change in transmission is smaller than in Fig. 4. For frequencies below the resonance (2, 2.5, and 3.1 THz), the pump-induced change in transmission is negative, while for frequencies at or above the resonance (3.9, 4.4, and 4.9 THz), the response is positive, with the largest increase observed at the resonant frequency. As explained below, the change in sign can be explained by a pump-induced red-shift of the plasmon frequency.

4. THEORY AND ANALYSIS

For the probe signal, which is polarized perpendicular to the ribbons, the transmission spectrum $\tau(\omega)$ can be well approximated

using a Drude-Lorentz model of the conductivity [22],

$$\frac{\tau(\omega)}{\tau_0} = \left| 1 + \frac{wZ_0}{\pi\Lambda(1+n_{\text{SiC}})} \frac{D}{\left(\Gamma - i \frac{\omega^2 - \omega_p^2}{\omega} \right)} \right|^{-2} \quad (1)$$

where w/Λ is the duty cycle of the graphene grating, $Z_0 (= \sqrt{\mu_0/\epsilon_0})$ is the vacuum impedance and n_{SiC} is the substrate refractive index. The plasmon resonance frequency, linewidth, and strength are described by ω_p , Γ , and D , respectively. As illustrated by the dashed theory curve in Fig. 2, this model accurately predicts the observed transmission spectrum for the graphene ribbons considered here. Eq. (1) is plotted in Fig. 5a, which shows specifically how the the linewidth, resonance frequency, and strength are related to the transmission spectrum.

The nonlinear response of the graphene ribbons can be explained by a two-temperature model, in which the optically excited carriers are heated to transient temperature T that exceeds the lattice temperature T_L . Because the electron-electron scattering time (approximately 10 fs in graphene) is much faster than the optical pulsewidths employed here, the optically excited carriers can be well characterized by a thermal distribution of hot carriers. All three of the Drude-Lorentz parameters appearing in Eq. (1) implicitly depend on the transient electron temperature T , according to:

$$D(T) \simeq D_0 \left(1 - \frac{\pi^2 k_B^2 T^2}{6\epsilon_F^2} \right) \quad (2)$$

$$\omega_p(T) \simeq \omega_{p0} \left(1 - \frac{\pi^2 k_B^2 T^2}{12\epsilon_F^2} \right) \quad (3)$$

$$\Gamma(T) \simeq \Gamma_0 \left(1 + \frac{\pi^2 k_B^2 T^2}{6\epsilon_F^2} \right) + \gamma T \quad (4)$$

The Drude weight, plasmon frequency and scattering rate scale with the chemical potential as μ , $\mu^{1/2}$, and μ^{-1} respectively, and the leading terms appearing in parentheses in Eq. (2)-Eq. (4) all arise from the temperature dependence of the chemical potential, which is expanded to second-order in $k_B T/\epsilon_F$. The additional term appearing in Eq. (4) describes a temperature-dependent increase in the LA phonon scattering rate. The factor γ appearing in this equation is proportional to the acoustic deformation potential, and is equal to $1.264 \times 10^{-3} \text{ K}^{-1} \text{ ps}^{-1}$ for the graphene considered here, as summarized in Table 1.

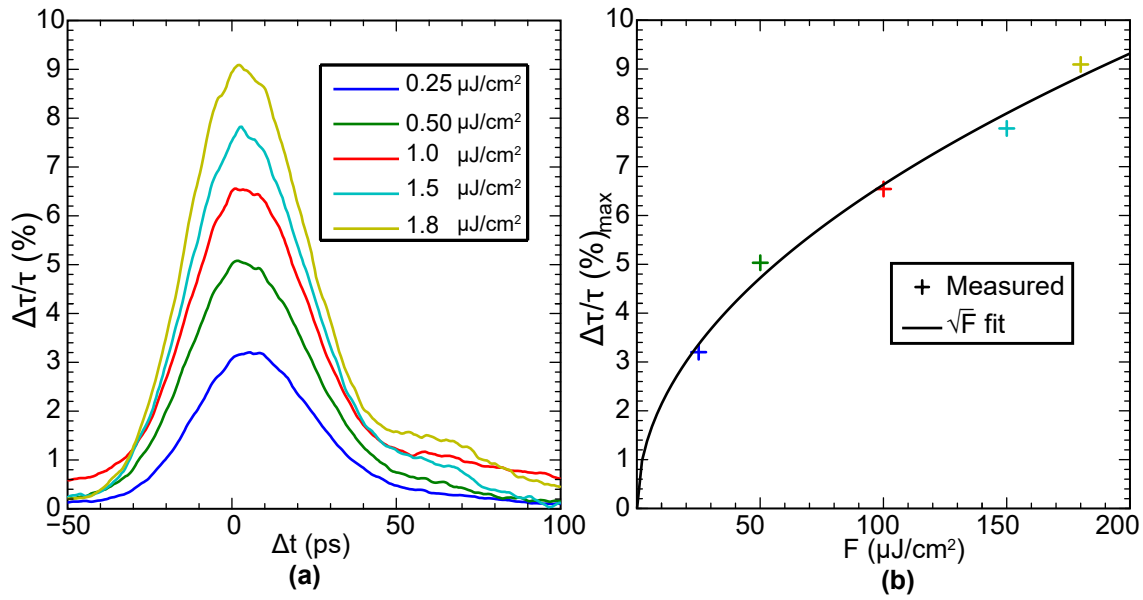


Fig. 3. (a) Pump-induced change in THz transmission, measured at the plasmon resonance of 3.9 THz, for a variety of pump fluences. (b) Peak change in transmission, as a function of the pump fluence, showing approximate square-root dependence (line).

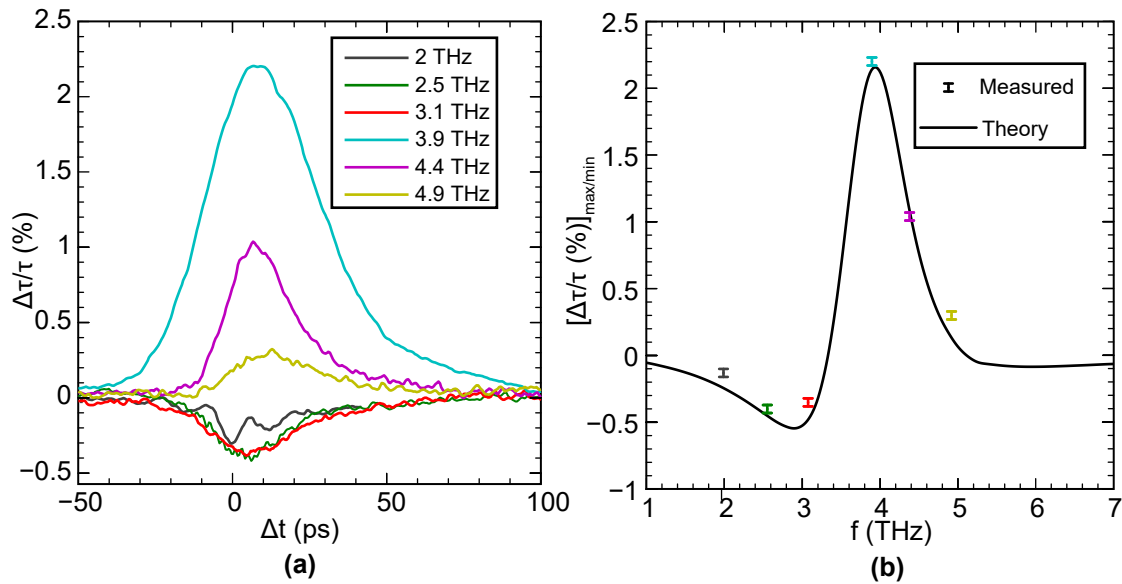


Fig. 4. (a) Differential probe transmission through the sample measured at frequencies above and below the plasmon resonance, for the case when the pump polarization is polarized parallel to the graphene ribbons, while the probe is polarized perpendicular. (b) Peak change in transmission as a function of the frequency. The crosses indicate the measurements presented in (a), the line is the result of the theoretical calculation based on a thermal model of hot electrons.

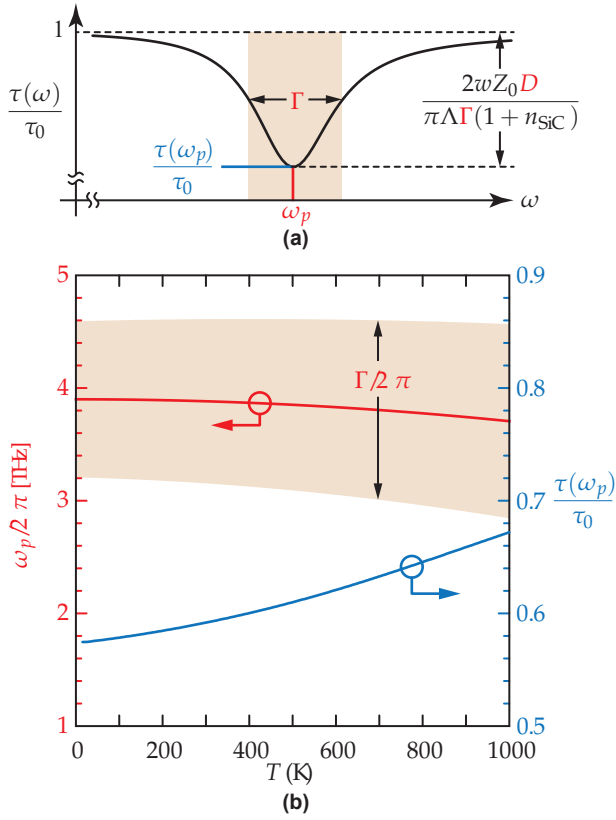


Fig. 5. (a) Transmission spectrum for graphene ribbons (Eq. (1)), normalized relative to that of a substrate with no graphene, obtained from the Drude Lorentz model of conductivity. The center frequency, width, and depth are related to the plasmon frequency ω_p , scattering rate Γ , and Drude weight D , respectively. These three parameters, indicated in red, are predicted to vary with the electron temperature T , as shown in (b).

Taken together, Eqs. (2)–(4) predict that when the electron temperature increases under THz illumination, the plasmon resonance will weaken, broaden, and red-shift to lower frequencies. Fig. 5b plots how the Drude weight, linewidth and plasmon frequency vary with the electron temperature. Fig. 6a plots the calculated transmission spectrum for electron temperatures up to 1000 K, calculated for the graphene conditions considered here, clearly showing this effect. The thermally-induced red shift causes the transmission to decrease for frequencies below the resonance, but increase above resonance, in agreement with the measurements presented in Fig. 4.

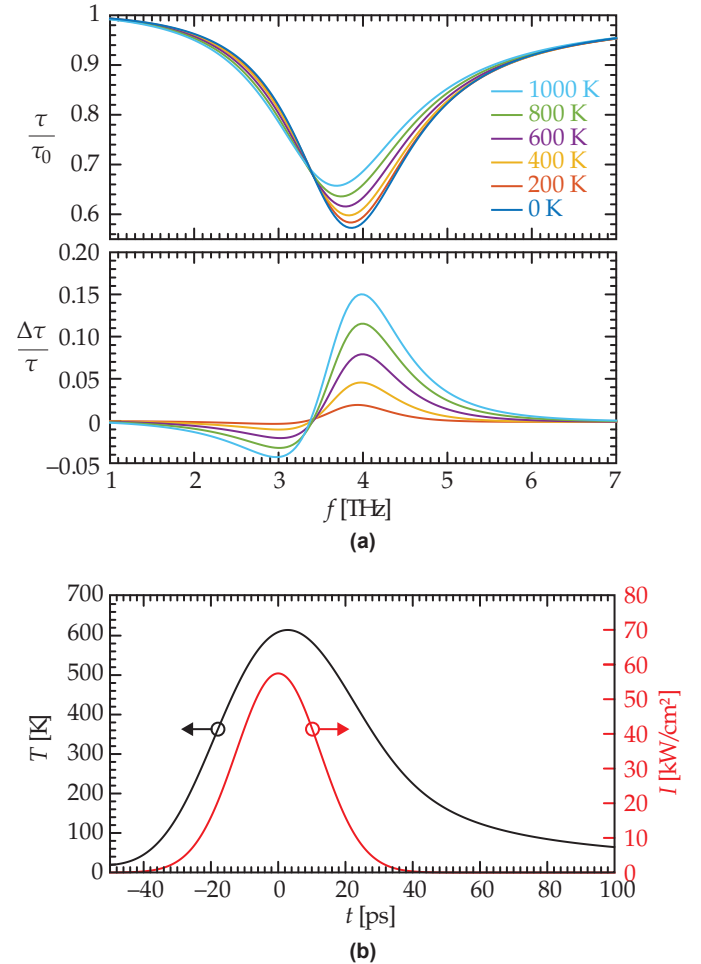


Fig. 6. (a) Upper: Calculated normalized transmission for electron temperatures up to 1000 K, showing the predicted red-shift of the plasmon when the electrons are heated. Lower: Corresponding fractional change in transmission $\Delta\tau/\tau$. (b) Calculated transient electron temperature as a function of time, together with the incident pulse intensity $I(t)$, for a $1.8 \mu\text{J cm}^{-2}$ Gaussian pulse of 29 ps duration (FWHM), for which the peak electron temperature reaches 610K. The corresponding multimedia file (Media 1) shows the dynamic temperature evolution, together with an animation illustrating the changes in the transmission spectrum.

To model the temporal evolution of the pump-induced change in transmission, we numerically solved the nonlinear

thermal equation[31]

$$\alpha T \frac{dT}{dt} + \beta(T^3 - T_L^3) = A(\omega, T)I(t) \quad (5)$$

where αT is the specific heat of graphene, β describes the disorder-assisted cooling coefficient of hot carriers[31, 32], $A(\omega, T)$ is the power absorption coefficient in the graphene film, and $I(t)$ is the incident pump intensity, which in these experiments describes a Gaussian pulse with a full width at half maximum (FWHM) of 29 ps. As summarized in Table 1, the two parameters α and β appearing in Eq. (5) are entirely determined by Fermi energy and mean free path (which characterizes the level of disorder in the sample.)

The timescale for hot-carrier cooling can be estimated by setting the right-hand side of Eq. (5) to zero, and assuming $T \gg T_L$, in which case Eq. (5) may be directly integrated to find

$$T(t) = \frac{T_0}{1 + \frac{\beta T_0}{\alpha} t} \quad (6)$$

where T_0 represents the peak (initial) electron temperature produced by the pump pulse. If we assume a peak temperature of $T_0 = 610$ K (the maximum level predicted for the experimental conditions considered here), the electrons will cool to half their initial temperature over a time of $\alpha/\beta T_0 = 8.8$ ps. Although the relationship between temperature and transmission is nonlinear, the timescale estimated here is consistent with the response time observed in the pump-probe measurements in Fig. 4a.

Fig. 6b plots the calculated electron temperature, obtained by solving Eq. (5), together with the incident pulse intensity $I(t)$, for a $1.8 \mu\text{J cm}^{-2}$ Gaussian pulse of 29 ps duration, for which the peak electron temperature is predicted to reach 610 K. The accompanying media file presents an animation showing the transient evolution of the transmission spectrum caused by this stimulus, showing both the spectral red-shift and broadening of the resonance.

Fig. 4b plots the peak differential change in transmission as a function of frequency for the five frequencies considered here. The solid line indicates the result predicted by numerically calculating the electron temperature $T(t)$ Eq. (5) and using Eqs. (1)-(4) to determine the consequent change in transmission. The experimental observations are in excellent agreement with the theoretical predictions, and clearly show evidence of the transient red-shift in the plasmon frequency.

The theoretical model used exclusively parameters taken or inferred from separately conducted measurements: the carrier concentration and plasmon linewidth were inferred from linear FTIR transmission measurements of patterned and unpatterned graphene in Fig. 2. The cooling coefficient β (and consequently the disorder mean-free path l) was chosen to match the power dependence in Fig. 3b. All of the remaining model parameters are derived from these, using well-defined relationships and accepted physical constants for graphene, as summarized in Table 1. The only adjustable parameter needed to match the data shown in Fig. 4b was that the absorbed pump power was reduced by a factor of approximately two relative to what was assumed in the co-polarized case. We believe that this discrepancy could be explained by the (unmeasured) difference in spatial overlap between the pump and probe between the two measurements, although we acknowledge that this could also be evidence of anisotropic thermal distribution of carriers.

The wavelength dependence of the nonlinear absorption allows employing graphene ribbons either as a saturable absorber

or saturable transmitter. The low heat capacity of the charge carriers in the graphene leads to a pronounced increase of the carrier temperature, even when excited at moderate fluence that is achievable with table-top sources. As the plasmon frequency of the ribbons can be tuned, either by changing the ribbon dimensions or by gating, graphene ribbons can feature a strong nonlinearity in a wide spectral range from THz to mid-infrared radiation. Even stronger nonlinearity is expected if higher quality graphene is used, or if additional longitudinal enhancement is introduced through a resonant cavity. As the carrier phonon cooling in graphene is very efficient, the pump-induced change in transmission is mostly limited to the duration of the pump pulse, which is consistent with pump-probe experiments on unpatterned graphene in this wavelength range. This makes the thermal nonlinearity in graphene ribbons suitable for ultrafast processes.

5. CONCLUSION

Graphene plasmons provide a platform for nonlinear THz materials that can be tailored to a desired wavelength. The low specific heat of the carriers in graphene, in combination with a fast thermal relaxation, leads to strong nonlinearities with a short life time of about 9 ps, even at moderate fluence that is achievable with table-top lasers sources. As the resonance frequency changes with temperature, an array of graphene ribbons can serve either as saturable absorber or saturable transmitter, depending on whether the photon frequency is below or at/above resonance, respectively. Adding up several layers of ribbons, the nonlinearity can be further enhanced.

FUNDING INFORMATION

Office of Naval Research (ONR) (N000141310865); National Science Foundation (NSF) (ECCS 1309750).

ACKNOWLEDGMENTS

The sample fabrication was carried out at the University of Maryland Nanocenter. Support from P. Michel and the FELBE-team is gratefully acknowledged.

REFERENCES

1. M. Breusing, S. Kuehn, T. Winzer, E. Malić, F. Milde, N. Severin, J. P. Rabe, C. Ropers, A. Knorr, and T. Elsaesser, "Ultrafast nonequilibrium carrier dynamics in a single graphene layer," *Phys. Rev. B* **83**, 153410 (2011).
2. J. M. Dawlaty, S. Shivaraman, M. Chandrashekar, F. Rana, and M. G. Spencer, "Measurement of ultrafast carrier dynamics in epitaxial graphene," *Appl. Phys. Lett.* **92**, 042116 (2008).
3. P. A. Obraztsov, M. G. Rybin, A. V. Tyurnina, S. V. Garinov, E. D. Obraztsova, A. N. Obraztsov, and Y. P. Svirko, "Broadband light-induced absorbance change in multilayer graphene," *Nano Lett.* **11**, 1540–1545 (2011). PMID: 21443162.
4. S.-Y. Hong, J. I. Dadap, N. Petrone, P.-C. Yeh, J. Hone, and R. M. Osgood, "Optical third-harmonic generation in graphene," *Phys. Rev. X* **3**, 021014 (2013).
5. N. Kumar, J. Kumar, C. Gerstenkorn, R. Wang, H.-Y. Chiu, A. L. Smirl, and H. Zhao, "Third harmonic generation in graphene and few-layer graphite films," *Phys. Rev. B* **87**, 121406 (2013).

ε_F	Fermi energy	350 meV
$n = \frac{1}{\pi} \left(\frac{\varepsilon_F}{\hbar v_F} \right)^2$	carrier concentration	$9.0 \times 10^{12} \text{ cm}^{-2}$
$\mu_c = \frac{ev_F}{\sqrt{\pi n \Gamma_0 \hbar}}$	carrier mobility	$3,600 \text{ cm}^2 \text{ V}^{-1} \text{ s}^{-1}$
w	graphene ribbon width	900 nm
Λ	graphene grating period	1200 nm
n_{SiC}	SiC substrate refractive index	3.5
$D_0 = \sqrt{\pi n e^2 v_F / \hbar}$	Drude weight	$0.13 \Omega^{-1} \text{ ps}^{-1}$
ω_{p0}	plasmon frequency	$2\pi \cdot (3.9 \text{ THz})$
$\Gamma_0 = \frac{ev_F}{\sqrt{\pi n \mu_c \hbar}}$	plasmon linewidth	8.7 ps^{-1}
T_L	lattice temperature	15 K
l	disorder mean free path	3 nm
$\alpha = 2\pi k_B^2 \varepsilon_F / (3\hbar^2 v_F^2)$	specific heat	$2.01 \times 10^{-9} \text{ J m}^{-2} \text{ K}^{-2}$
$\beta = \zeta(3) V_D^2 \varepsilon_F k_B^3 / (\pi^2 \rho \hbar^4 v_F^3 s^2 l)$	supercollision cooling coefficient	$0.37 \text{ W m}^{-2} \text{ K}^{-3}$
$\gamma = \frac{k_B V_D^2 \varepsilon_F}{4\hbar^3 v_F^3 \rho s^2}$	LA phonon scattering coefficient	$1.26 \times 10^{-3} \text{ K}^{-1} \text{ ps}^{-1}$

Table 1. Summary of numerical, physical, geometrical and experimental parameters and conditions. The expressions given here use the following accepted physical constants for graphene: $v_F = 10^6 \text{ m s}^{-1}$ represents the Fermi velocity, $V_D = 10 \text{ eV}$ is the acoustic deformation potential, $\rho = 7.6 \times 10^{-7} \text{ kg m}^{-2}$ is the density, and $s = 2.1 \times 10^4 \text{ m s}^{-1}$ is the acoustic velocity.

6. E. Hendry, P. J. Hale, J. Moger, A. K. Savchenko, and S. A. Mikhailov, "Coherent nonlinear optical response of graphene," *Phys. Rev. Lett.* **105**, 097401 (2010).
7. T. Gu, N. Petrone, J. F. McMillan, A. van der Zande, M. Yu, G. Q. Lo, D. L. Kwong, J. Hone, and C. W. Wong, "Regenerative oscillation and four-wave mixing in graphene optoelectronics," *Nat. Photon.* **6**, 554–559 (2012).
8. Q. Bao, H. Zhang, Y. Wang, Z. Ni, Y. Yan, Z. X. Shen, K. P. Loh, and D. Y. Tang, "Atomic-Layer Graphene as a Saturable Absorber for Ultrafast Pulsed Lasers," *Adv. Funct. Mater.* **19**, 3077–3083 (2009).
9. H. Zhang, D. Y. Tang, L. M. Zhao, Q. L. Bao, and K. P. Loh, "Large energy mode locking of an erbium-doped fiber laser with atomic layer graphene," *Opt. Express* **17**, 17630–17635 (2009).
10. S. Winnerl, M. Orlita, P. Plochocka, P. Kossacki, M. Potemski, T. Winzer, E. Malic, A. Knorr, M. Sprinkle, C. Berger, W. A. de Heer, H. Schneider, and M. Helm, "Carrier relaxation in epitaxial graphene photoexcited near the dirac point," *Phys. Rev. Lett.* **107**, 237401 (2011).
11. H. Y. Hwang, N. C. Brandt, H. Farhat, A. L. Hsu, J. Kong, and K. A. Nelson, "Nonlinear thz conductivity dynamics in p-type cvd-grown graphene," *The J. Phys. Chem. B* **117**, 15819–15824 (2013). PMID: 24102144.
12. G. Jnawali, Y. Rao, H. Yan, and T. F. Heinz, "Observation of a transient decrease in terahertz conductivity of single-layer graphene induced by ultrafast optical excitation," *Nano Lett.* **13**, 524–530 (2013). PMID: 23330567.
13. Z. Misc, K.-J. Tielrooij, K. Parvez, S. A. Jensen, I. Ivanov, X. Feng, K. Müllen, M. Bonn, and D. Turchinovich, "Thermodynamic picture of ultrafast charge transport in graphene," *Nat. Commun.* **6**, 7655 (2015).
14. H. A. Hafez, S. Kovalev, J.-C. Deinert, Z. Mics, B. Green, N. Awari, M. Chen, S. Germanskiy, U. Lehnert, J. Teichert, Z. Wang, K.-J. Tielrooij, Z. Liu, Z. Chen, A. Narita, K. Müllen, M. Bonn, M. Gensch, and D. Turchinovich, "Extremely efficient terahertz high-harmonic generation in graphene by hot dirac fermions," *Nature*. (2018).
15. H. A. Atwater and A. Polmann, "Plasmonics for improved photovoltaic devices," *Nat. Mater.* **9**, 205–213 (2010).
16. M. Kauranen and A. V. Zayats, "Nonlinear plasmonics," *Nat. Photonics* **6**, 737–748 (2012).
17. F. H. L. Koppens, D. E. Chang, and F. J. García de Abajo, "Graphene plasmonics: A platform for strong light-matter interactions," *Nano Lett.* **11**, 3370–3377 (2011).
18. L. Ju, B. Geng, J. Horng, C. Girit, M. Martin, Z. Hay, H. A. Bechtel, X. Liang, A. Zettl, Y. R. shen, and F. Wang, "Graphene plasmonics for tunable terahertz metamaterials," *Nat. Nanotechn.* **6**, 630–634 (2011).
19. A. N. Grigorenko, M. Polini, and K. S. Novoselov, "Graphene plasmonics," *Nat. Photon.* **6**, 749–758 (2012).
20. T. Low and P. Avouris, "Graphene plasmonics for terahertz to mid-infrared applications," *ACS Nano* **8**, 1086–1101 (2014).
21. F. Hu, Y. Luan, Z. Fei, I. Z. Palubski, M. D. Goldflam, S. Dai, J.-S. Wu, K. W. Post, G. C. A. M. Janssen, M. M. Fogler, and D. N. Basov, "Imaging the localized plasmon resonance modes in graphene nanoribbons," *Nano Lett.* **17**, 5423–5428 (2017).
22. M. M. Jadidi, J. C. König-Otto, S. Winnerl, A. B. Sushkov, H. D. Drew, T. E. Murphy, and M. Mittendorff, "Nonlinear terahertz absorption of graphene plasmons," *Nano Lett.* **16**, 2734–2738 (2016).
23. J. D. Cox and F. J. G. de Abajo, "Transient nonlinear plasmonics in nanostructured graphene," *Optica*. **5**, 429–433 (2018).

24. C. Riedl, C. Coletti, and U. Starke, "Structural and electronic properties of epitaxial graphene on sic (0 0 0 1): a review of growth, characterization, transfer doping and hydrogen intercalation," *J. Phys. D: Appl. Phys.* **43**, 374009 (2010).
25. J. D. Emery, V. D. Wheeler, J. E. Johns, M. E. McBriarty, B. Detlefs, M. C. Hersam, D. Kurt Gaskill, and M. J. Bedzyk, "Structural consequences of hydrogen intercalation of epitaxial graphene on SiC(0001)," *Appl. Phys. Lett.* **105**, 161602 (2014).
26. K. M. Daniels, M. M. Jadidi, A. B. Sushkov, A. Nath, A. K. Boyd, K. Sridhara, H. D. Drew, T. E. Murphy, R. L. Myers-Ward, and D. K. Gaskill, "Narrow plasmon resonances enabled by quasi-freestanding bilayer epitaxial graphene," *2D Mater.* **4**, 025034 (2017).
27. P. Avouris and C. Dimitrakopoulos, "Graphene: synthesis and applications," *Mater. Today* **15**, 86 – 97 (2012).
28. F. Speck, J. Jobst, F. Fromm, M. Ostler, D. Waldmann, M. Hundhausen, H. B. Weber, and T. Seyller, "The quasi-free-standing nature of graphene on H-saturated SiC(0001)," *Appl. Phys. Lett.* **99**, 122106 (2011).
29. J. L. Tedesco, B. L. VanMil, R. L. Myers-Ward, J. M. McCrate, S. A. Kitt, P. M. Campbell, G. G. Jernigan, J. C. Culbertson, C. R. Eddy, and D. K. Gaskill, "Hall effect mobility of epitaxial graphene grown on silicon carbide," *Appl. Phys. Lett.* **95**, 122102 (2009).
30. M. M. Jadidi, A. B. Sushkov, R. L. Myers-Ward, A. K. Boyd, K. M. Daniels, D. K. Gaskill, M. S. Fuhrer, H. D. Drew, and T. E. Murphy, "Tunable terahertz hybrid metal-graphene plasmons," *Nano Lett.* **15**, 7099–7104 (2015).
31. J. C. W. Song, M. Y. Reizer, and L. S. Levitov, "Disorder-assisted electron-phonon scattering and cooling pathways in graphene," *Phys. Rev. Lett.* **109**, 106602 (2012).
32. J. K. Viljas and T. T. Heikkilä, "Electron-phonon heat transfer in monolayer and bilayer graphene," *Phys. Rev. B* **81**, 245404 (2010).